DETECTION OF EL NIÑO-SOUTHERN OSCILLATION (ENSO)-INDUCED CHANGES BASED ON ANALYSES OF MULTITEMPORAL EARTH OBSERVATION DATA: A STUDY FROM NW PERU

Veronika KOPAČKOVÁ*[1], Michal RAJCHL[1], Jan HARBULA[1], František LAUFEK[1], Daniel NÝVLT[1], Tomáš HROCH[1], Hanuš JAN[1]

[1]Czech Geological Survey, Klárov 3, 118 21, Prague 1, Czech Republic
[2]Institute of Systems Biology and Ecology of the Academy of Sciences of the Czech Republic, Na Sádkách 7, České Budějovice, Czech Republic
*veronika.kopackova@seznam.cz; phone: +420/606 547 908; fax: 1 +420/257 531 376

ABSTRACT

The Sechura desert, in the northern part of Peru, represents a unique system characterized by minimum precipitation and therefore all the surface water input is regulated by the two rivers, the Chira and the Piura, draining water from the Andean part of their catchments. Water inflow in these two rivers is controlled by seasonal precipitation changes typical for the dry and wet seasons. Once in every decade, this relatively steady system is affected by a phenomenon that is known as the El Niño/Southern Oscillation (ENSO). The wet weather conditions normally present over the western Pacific move to the east and bring heavy rainfalls that, as a consequence, bring enormous water inflow for the Chira and Piura rivers. River fluvial systems respond to these extremes by unpredictable changes in the geometry and positions of the river channels. The present study covers a total area of 20 000 km^2 and combines various mapping techniques while utilizing diverse Earth Observation data: (a) multitemporal Landsat scenes from 1973, 1984, 1985 and 2000-2001; (b) 6 scenes of ASTER acquired during 2006-2007. Multitemporal Landsat scenes were used to reconstruct the fluvial networks of the Chira and Piura Rivers and to classify surface material in the desert environment. Analysis of ASTER TIR scenes allowed creation of a mineral abundance map of quartz-rich, carbonate-rich and gypsum-rich sediments. The results derived from a study utilizing diverse and multitemporal Earth Observation data provided key information that enabled a synoptic change detection assessment of the lower-catchments areas of the Chira and Piura Rivers in the Sechura desert during the past three decades.

MOTS CLÉS

multitemporal analysis, emissivity ratios, land cover, Sechura desert, NW Peru, Landsat, ASTER TIR, ENSO..

Article remis le 6 février 2009, accepté définitivement le 1er septembre 2009.

1. INTRODUCTION

The quasi-periodic alterations of the climate in South America and of the oceanographic conditions in the eastern Pacific Ocean, referred to as the «El Niño» phenomenon, are part of a global anomaly in the ocean-atmosphere interactive system (the El Niño-Southern Oscillation, ENSO). The ENSO system is commonly considered to be the best example of ocean/atmosphere interaction and one of the most relevant manifestations of interannual variability in the global climate system. Although the ENSO phenomenon is primarily observed in the equatorial Pacific Ocean and the bordering land areas, it has been shown that it induces worldwide climatic anomalies (teleconnections) in tropical and extra-tropical areas (Barnett, 1981; Horel and Wallace, 1981; Rasmusson, 1985; Ropelewski and Halpert, 1987; Kiladis and Diaz, 1989).

The main climate anomalies that characterize the E1 Niño phenomenon in South America are related to a modification of the Walker circulation and to a southern shift of the Intertropical Convergence Zone. They include exceptional precipitation in the normal and semi-arid coastal regions of northwestern Peru and southernmost Ecuador (Waylen and

Caviedes, 1986) and, on the other hand, significant rainfall deficits in the Altiplano of southeastern Peru and Bolivia, the Brazilian northeast, northernmost South America and southern Central America (Caviedes, 1973, 1975, 1984, Hastenrath and Heller, 1977; Francou and Pizarro, 1985; Ropelewski and Halpert, 1987; Aceituno, 1987, 1988; Rogers, 1988; Quinn and Neal, 1992).

The impacts of the El Niño phenomenon along the whole western coast of South America are documented by catastrophic rainfalls and associated river floods, records of lake salinity variations, beach ridge sequences and numerous indications of alterations in the biotic and physical coastal environment. These characteristics and the fact that many impacts and consequences of the ENSO/EI Niño anomalies are catastrophic explain why the phenomenon has received particular attention in major current research programs (1GBP-»Global Change», Research Program on the World Climate, Tropical Ocean-Global Atmosphere project, etc.).

Recently, remote sensing data have been used in solving various earth related problems by processing the remotely sensed digital images. Extensive use has been made of the Landsat series of sensors (Multispectral Scanner - MSS; Thematic Mapper - TM; and Enhanced Thematic Mapper Plus - ETM+) to characterize diverse sediments and land use/cover changes in arid regions (Liberti *et al.*, 2009; Small *et al.*, 2009; Berberoglu and Akin, 2009). The Landsat series of sensors has also provided a rich historical database extending since 1972; therefore the archive data can be used to detect landscape changes after catastrophic events. In contrast to very good temporal resolution (repeat cycle of Landsat: 16 days for WGS 2 and 18 days for WGS 1), Landsat has fairly low spectral resolution, the instrument covers 185 by185 km with seven broad spectral bands. Six of the bands (30 m pixel) detect reflected visible and infrared radiation (0.45 to 2.35 μm). Additionally, there are one to two thermal infrared bands for TM and ETM+, respectively.

Therefore, data from the NASA Earth Observing System (EOS) satellite-based instruments provides an opportunity to collect information with high spatial, spectral, and temporal resolution and extend geological applications and the ability to detect diverse rocks and minerals in arid regions (Katra and Lancaster, 2008). The Advanced Spaceborne Thermal Emission and Reflection Radiometer (ASTER) instrument acquires surface data in the visible to near infrared (VNIR: three bands, 15 m pixel), shortwave infrared (SWIR: six bands, 30 m pixel), and thermal infrared (TIR: five bands, 90 m pixel) wavelength regions of the electromagnetic spectrum (Abrams, 2000).

This paper addresses the problem of classification of the major sediment types from the Sechura desert, NW Peru, based on multitemporal and multisensor satellite data (e.g., Landsat MSS, Landsat TM/ETM+, ASTER TIR) to detect ENSO-induced changes by analyzing the after- and between-event images. An episodic influx of surface water affects not only the extent of the moist areas, lakes and river beds but also the surface mineral composition (e.g., evaporite evolution, clastic material transport to ephemeral lakes and consequent aeolian dust transport). The uniform classification technique was applied to systematically analyze the Landsat time-series images to delineate water network/water bodies and to define the extent of these geological classes as evaporites, siliciclastics, bioclastics, nonactive surface (e.g., crystalline bedrock, ancient aeolian sediments) and aeolian material in a mixture with the other rocks. Furthermore, we have made an effort to differentiate between quartz-rich and carbonate-rich rocks as well as evaporites by calculating several mineralogical indices, including the Quartz Index (QI) (Hewson *et al.*, 2005), Carbonate Index (CI) (Ninomia and Fu, 2002) and Gypsum Index (GyI), which we newly developed for our study, from ASTER TIR data acquired in 2006/2007.

ASTER VNIR and SWIR bands were not utilized, as they require calibration techniques different from that were applied in the present work. However, ASTER VNIR and SWIR bands will be utilized in a future study.

2. REGIONAL SETTING

The Sechura Desert is one of the biggest deserts in South America. It extends in northwestern Peru between the Andes Mts. and the Pacific margin. The desert is 280 km long and approximately 90 km vide, with a maximum width of 180 km. This area is relatively flat, with elevation ranging between 0 and 150 m above the sea level. Only isolated crystalline massifs have higher elevation (**Plate 1, page …**). The Sechura Desert was formed in the area of the emerged Talara and Sechura forearc basins. Marine regression began during the Pliocene and has continued up to present. Individual regressive stages are indicated by a system of terraces and palaeocoastlines.

The local climate is influenced by the Andean Mountain Range and the cold Humboldt ocean current (also called the Peruvian current). The Andean Mountain Range blocks precipitation transfer from the Amazon and the cold Humboldt current is responsible for reverse temperature stratification, as it generates significant cloudiness and blocks the intertropical convergence zone in this part. This very dry and warm climate is present in the area

between the cities of Piura and Tumbes, on the north-western coast of Peru. The situation changes from December to April as result of the summer warming of Pacific costal waters but a dramatic change appears mainly during the ENSO event, when the temperature increase of surface oceanic water is more significant. Rainstorms, typical for the intertropical convergence zone, bring enormous amounts of surface water that cause significant damages to the infrastructure, agriculture and other areas of human activities as well.

The north-western part of Peru is affected by strong El Niño rainfalls approximately once in 7-10 years, however, in the past 150 years, there have been very strong events in 1891, 1926, 1982/83 and 1997 and a rather strong event also occurred in 1973 (Rein, 2007).

The present morphology of the desert was formed by exodynamic processes that are predominantly represented by erosional/accumulative activity of generally ephemeral streams and rivers, and by aeolian activity. The most important geomorphological agents in the desert are the two rivers (Chira and Piura), that originate in the Andes Mts., and a system of endorheic depressions dominated by sabkha environment, where seasonal lakes are formed during flooding (**Plate 1, page …**). The Chira river flows in a relatively narrow valley, whereas the Piura River forms a quite flat fluvial fan in the lowest part of its catchment. The area of this fan is characterised by significant changes of the river channel during the ENSO events (Rajchl *et al.*, 2008).

Dune fields that are locally developed in the desert area are fed by sandy material coming from the Pacific coast and also by material coming from the ephemeral lakes. Significant portions of these fields are destroyed by flooding.

3. MATERIAL SAMPLING AND ANALYSIS

Over 100 points distributed within the large study area were documented in the field. In 18 selected points that represented all the major sediment genesis types (e.g., sediments of fluvial, alluvial, aeolian and oceanic origin), surface material (0-2 cm depth) was collected to examine the mineralogy using X-Ray diffraction and to study the reflectance properties using an ASD FieldSpec 3® portable spectroradiometer.

The ASD instrument uses three separate spectrometers to measure the radiance between wavelengths of 0.350 µm and 2.500 µm. Five individual scan spectra were averaged for each output spectrum. Radiance spectra were normalized against a 99% Spectralon® white reference to produce relative reflectance spectra for each measurement. A common laboratory set-up was used for all the measurements with an aperture-target distance set at 15 cm, corresponding to a nominal area of 5 cm on the target. Illumination was provided by a halogen bulb and was fixed at a distance of 80 cm directed at the target from an elevation angle of 45°. The effect of the sediment mineralogical composition on the spectral properties was studied (**Fig. 1**) to choose a suitable band rationing method for broadband Landsat images (see chapter 5.1.1.) and to enable discrimination of different sediment types in the study area.

4. DATA LAYER PREPARATION

Data used for this study include 10 MSS and TM/ETM+ Landsat scenes (**Table 1**), 6 ASTER scenes (**Table 2**), 1:100, 000 scale topographic and geological maps (Palacios, 1994; Caldas *et al.,* 2000).

ACQUSITION DATE	SENSOR	MOSAIC NAME	SCENE NAME
17.03.1973	MSS	MSS_1973	LM1011063007307690
17.03.1973	MSS		LM1011064007307690
12.01.1984	MSS	MSS_1984	LM4011064008401210
13.01.1984	MSS		LM4011064008401810
03.09.1985	TM5	TM5_1985	LT5011063008524650_WO
05.10.1985	TM5		LT5011064008527850_WO
20.01.1990*	TM5	TM5_1990	p011r063_1990
20.01.1990*	TM5		p011r064_1990
25.12.2000*	TM7 ETM+	TM7_2000-2001	p011r063_7k20001225_z16
11.02.2001*	TM7 ETM+		p011r064_7k20010211_z17

Table 1. *List of the Landsat data used for the study (downloaded scenes marked with*). (MSS = Multispectral Scanner, TM = Thematic Mapper, ETM = Enhanced Thematic Mapper).*

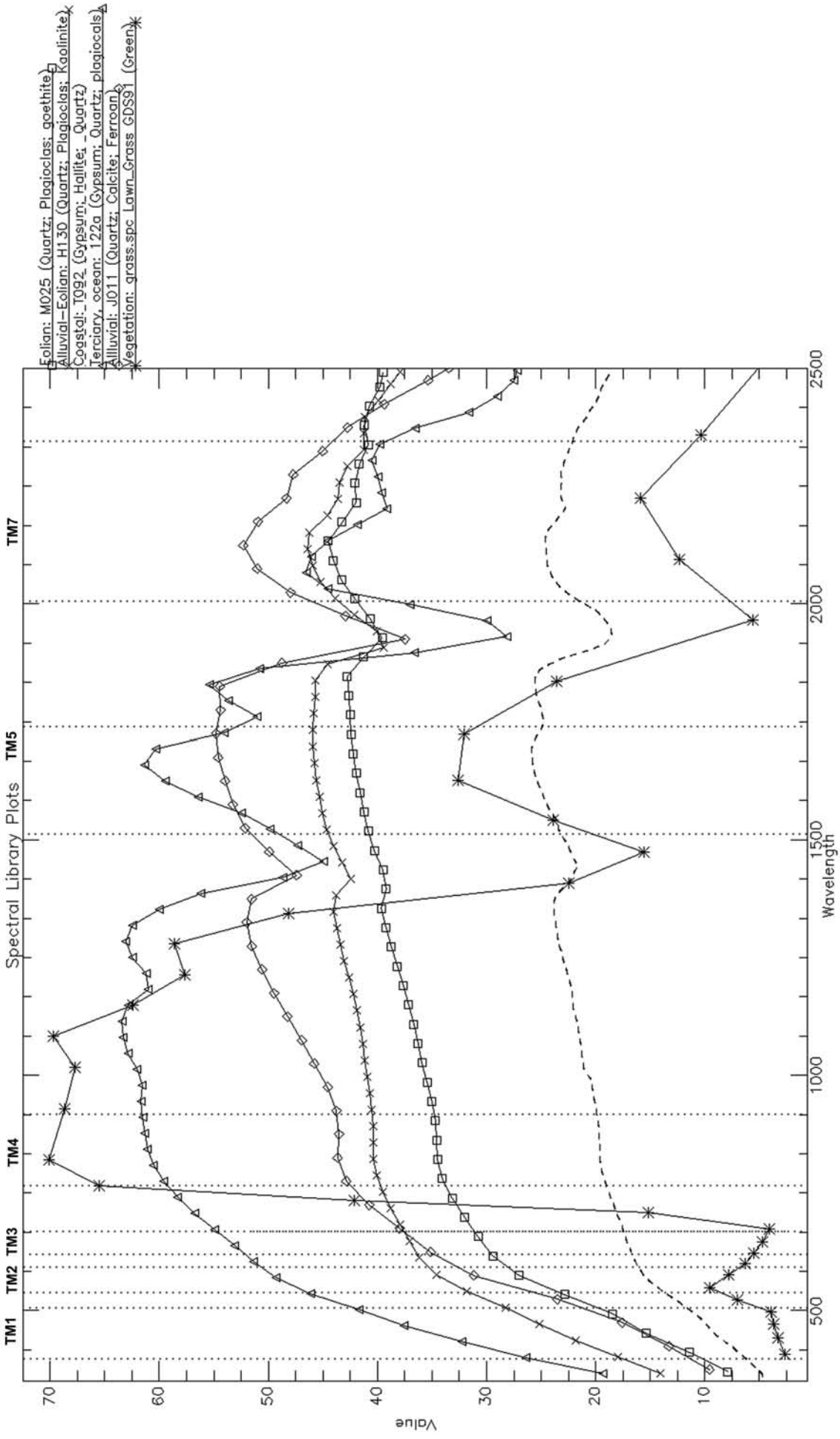

Figure 1 : *Laboratory reflectance spectra of the selected sediment samples.*

ACQUSITION DATE	MOSAIC NAME	SCENE NAME
16.05.2006	As_16_05_2006	AST14DMO_00305162006155036_20070807112146_12216
16.05.2006		AST14DMO_00305162006155045_20070807112246_12344
25.05.2006	As_25_05_2006	AST14DMO_00305252006154431_20070807112457_12588
25.05.2006		AST14DMO_00305252006154440_20070807112457_12590
04.01.2007	As_04_01_2007	AST14OTH_00301042007154506_20071023110018_19346
04.01.2007		AST14OTH_00301042007154515_20071023105248_18210

Table 2. *List of the ASTER data used for the study.*

The Landsat data were chosen to document the situation after the strong El Niño events in 1973, 1982/83 and 1997 (Landsat data acquired in 1973, 1984 and 1985, 2000) and also the dry period of the ENSO cycle (Landsat data acquired in 1990). Some of the Landsat scenes were downloaded from the Global Land Cover Facility web site at Maryland (http://glcf.umiacs.umd.edu/index.shtml); the rest of the archive Landsat data was purchased from the U.S. Geological Survey. ASTER orthorectified archive data (DMO product available from the U.S. Geological Survey) acquired in 2006 and 2007 (Tab. 2) were also used for this study.

4.1. Orthorectification

Image-to-image geometric referencing was carried out to ensure co-location of the historical and recent images. All the Landsat images (MSS, TM and ETM$^+$) were orthorectified and geocoded to the Universal Transverse Mercator (UTM) coordinate system by using SRTM DEM (level 3). A minimum of 12 regularly distributed ground control points (GCPs) were identified in the images. Resampling was performed using a nearest neighbor algorithm. The transformation had a root mean square (RMS) error of up to 0.5 pixels, indicating that the image was accurate to within one pixel.

4.2. Seamless mosaic creation

The Landsat MSS/TM footprint is approximately 180×180 km^2; the ASTER footprint is only 60×60 km^2 and therefore it was necessary to combine multiple scenes into a mosaic for complete coverage of our large study region in the Sechura desert. Two orthorectified Landsat scenes with a minimum cloudiness acquired either at the same time or at the closest possible date were stitched together to create seamless Landsat mosaics for 1973 (MSS), 1984 (MSS), 1985 (TM), 1990 (TM) and 2000-2001 (ETM$^+$) (**Table 1**).

Creating a seamless mosaic from multitemporal ASTER data is a more complex issue. No detailed description or evaluation has been provided for the pre-processing issues and mosaicking strategy for TIR radiance data. Few published studies of ASTER data have been used in a multi-scene capacity (Hewson *et al.*, 2005; Scheidt *et al.*, 2008). The seamlessness of a mosaic is beneficial for displaying large regions; on the other hand, appending together radiometrically non-normalized scenes hinders spectral analysis and geological interpretation (e.g., detection of the surface composition). The thermal radiance received by the ASTER sensor is affected by the emissivity (composition) and temperature of the emitting surface. Therefore, three seamless mosaic stripes (**Table 2**) were created instead of one while stitching together only scenes with the same date of acquisition. An atmospheric correction was applied to the ASTER scenes after mosaicking.

4.3. Atmospheric correction of ASTER TIR data

The radiation emitted from a surface in the TIR spectral region is a function of the surface parameters (e.g., emissivity and temperature) and atmospheric parameters (e.g., evaporation and wind). The emissivity is related to the surface composition and can thus be used in arid regions for surface mineral mapping. Thermal atmospheric correction is used to approximate and remove the atmospheric contributions to thermal infrared data and it is recommended to perform this correction before converting the radiance data to emissivity.

We used the ISAC (In-Scene Atmospheric Compensation) algorithm to atmospherically correct the ASTER TIR data. The ISAC algorithm was described by Johnson (1998) and Young (1998) and was briefly reiterated by Kirkland *et al.* (2002), Vaughan *et al.* (2003) and Bassani et al. (2006).

The main atmospheric effects on TIR radiance include atmospheric absorption, downwelling atmospheric irradiance, and upwelling atmospheric path radiance. The ISAC algorithm assumes that the atmosphere is uniform over the data scene and that a near-blackbody surface exists within the scene. Neither the location of the blackbody nor the

temperature is known and required for this correction. All the atmospheric parameters are assumed to be homogenous across the image.

A single layer approximation of the atmosphere is used. The algorithm first determines the wavelength that most often exhibits the maximum brightness temperature and uses it as the reference wavelength. Only spectra that have their brightest temperature at this wavelength are used to calculate the atmospheric compensation. At this point, for each wavelength, the reference blackbody radiance values are plotted against the measured radiances and a line is fitted to the highest points in these plotted data. A weighted fit is assigned to weight regions with denser sampling. The compensation for this band is then applied as the slope and offset derived from the linear regression of these data with the computed blackbody radiances at the reference wavelength.

The atmospheric upwelling radiance and transmission are approximated using the following technique. First, the surface temperature of every pixel is estimated from the data and used to approximate the brightness temperature using the Planck function and assuming an emissivity of 1. Next, a line is fitted to a scatter plot of radiance vs. the brightness temperature. The atmospheric upwelling radiance and transmission are then derived from the slope and offset of this line.

5. DATA INTEGRATION AND ANALYSIS

The ultimate objective of our study was to use multitemporal and multisensor (Landsat MMS, TM and ETM$^+$; ASTER) remotely sensed imagery to understand geomorphologic and lithologic changes on synoptic scales. This might allow us to answer several questions about the effect of the El Niño phenomena on fluvial and aeolian cover dynamics in the Sechura desert. Apart from the original satellite image bands, diverse spectral enhancements have been tested to improve the identification of geological (e.g., rock types, mineral content) and morphological features (e.g., Chira and Piura fluvial networks), while taking into account the differences in the spectral resolution of the multi-sensor data used in this study. The methods used are summarized on the flow chart in **Plate 2, page ….**

5.1. Landsat data analysis

5.1.1. Landsat TM enhancement - band rationing method

Band rationing is a very simple and powerful technique in remote sensing. The basic concept of this technique lies in emphasizing or exaggerating an anomaly of the target object (Abrams,1983) while enhancing spectral differences between rocks and suppressing topographic effects (Dewidar, 2000; Sabins, 1987). The method divides pixels in one image by the corresponding pixels in a second image. Dividing one spectral band by another produces an image that provides relative band intensities. The resulting ratio images enhance the spectral differences between bands and clearly portray the variations of slope of spectral curves between two bands involved and are independent of the absolute pixel values.

We studied spectral property of the collected sediment samples (**Figure 1**) to select those TM band ratios that allowed the best discrimination among the sediment types. The absorption features related to clay minerals (mainly kaolinite), calcite, gypsum, Fe-Mg clorite (e.g., ferroan) and goethite were observed.

The ratio of TM band 5/7 (band 5: 1.55-1.75 μm; band 7: 2.08-2.35 μm) was used as a measure of the intensity of the vibrational absorptions in the 2.2 to 2.4 μm region and enabled mapping sediments rich in clay minerals (absorption in 2.206 μm) and carbonates (absorption in 2.340 μm). Additionally, this band ration emphasizes also gypsum-rich sediments as they show very high reflection in band TM5 and smaller absorption in TM7 (**Figure 1**). All these minerals were identified as a part of mixtures in alluvial, fluvial and ocean-origin sediments.

The TM 5/4 ratio was used to detect minerals characteristic with ferrous-ion crystal field absorption. Fe-bearing aluminosilicates cause a flat or concave-upward spectral reflectance pattern in the TM band 4 wavelength region (0.76 - 0.90 μm). The slope of the near-infrared spectra between 1 and 2 μm is controlled by these ferrous-related absorptions in Fe-bearing aluminosilicates (Sultan *et al.*, 1987). In our case, the only ferrous mineral identified in the collected sediment samples was Ferroan (Fe-Mg chlorite, also called Clinochlore-1MIIb). This mineral was detected in calcite-rich sediments and the product of 5/4 ratio highlighted this particular lithological type.

The electron transition in $Fe3^+$ typical for ferric minerals causes a strong absorption centered around 0.5 μm and a broad absorption at wavelengths greater than 0.95 μm, respectively (Bishop and Murad, 1996). The ratio of TM band 3 to band 1 (3/1) employs the reflection (TM3: 0.63 - 0.69 μm) and absorption (TM1 band: 0.45 - 0.52 μm) bands and helps to highlight ferric-rich lithologies.

XRD analysis proved that goethite was a typical mineral found in the eolian sediments, therefore the band ration 3/1 was used to detect this type of sediments.

To enhance the natural and cultivated vegetation, we used the Normalized Difference Vegetation Index (NDVI) because of its advantages (strong correlation with vegetation parameters, simplicity in calculation and interpretation) (Bastiaanssen, 1998). The NDVI provides a gross measure of relative photosynthetically active vegetation abundance per pixel as a ratio of visible red and near infrared reflectance. Actively photosynthesizing terrestrial vegetation typically exhibits low reflectance in the visible red and high reflectance in the near infrared wavelengths. The NDVI index (TM4 – TM3 / TM4 + TM3) was used to highlight the abundant green photosynthesising vegetation, which in our case was mostly agriculture and irrigated vegetation.

5.1.2. Landsat TM enhancement - texture analysis

In our study, detection of features that represent significantly distinct values from the surrounding pixels in an image, (e.g., river network) and discrimination of surfaces with variations in roughness (e.g., dune fields, coars-grained clastics) was highly useful. Texture analysis allowing a detection of these features by assigning them either positive or negative values can be beneficial. Although a texture analysis is particularly applicable to radar data, it has also been found to be useful in the enhancement of VIS/IR image data. We employed four different texture algoritms (Iron and Peterson, 1981): the mean Euclidean distance (1st-order transformation), the variance (2nd-order transformation), the skewness (3rd-order transformation) and kurtosis (4th-order transformation) to the NIR/SWIR TM bands (TM4, TM5, TM7). The best result was achieved in discrimination among the topographic features and the variability of surface roughness by applying the mean Euclidean distance algorithm to a TM 5 SWIR band.

TM band 5 is known to be sensitive to moisture in soil and vegetation. Salzano *et al.* (2008) used TM5 band for discrimination of snow, furthermore different snow types were classified (e.g., fresh snow, wind crust, snow with faceted crystals, unclassified, sun face surface). In our study, a texture image derived from TM5 emphasized differences among the sediment types which have sifnificantly different physical property (e.g., moisture, roughness and sparse vegetation cover on sediments): sediments of fluvial fans, dry aeolian sediments, bioclastic sediments and crystalline bedrock.

5.1.3. Landsat TM enhancement - PCA

Principal component analysis (PCA) is a mathematical transformation widely used to enhance multispectral image data. It has been employed in studies dealing with subjects such as discrimination ability among diverse terrestrial materials (Dewidar and Frihy, 2003), visualization of land use/land cover changes without any further enhancement processes (Dewidar, 2004), and irrigated land inventories (Visser, 1989; Lourens, 1990).

The method has been primarily used to compress the multispectral information into the first three principal components (PC1, PC2 and PC3) by calculating a new coordinate system in which the first new axis (the first principal component, PC1) maximizes the variance of the data along that axis. The second principal component (PC2) is orthogonal to the first one and has the second greatest variance, and so on. The data are decorrelated and it was found that most of the image variance is confined to the first few channels. After using this transformation, most of the information can be simultaneously displayed using the screen's color model (R, G, B = PC1, PC2, PC3).

By transforming DN distributions around sets of new multispaced axes, PCA produces totally uncorrelated images (Eklundh and Singh, 1993). It should also be emphasized that PCA does not reduce the amount of information and each PC grouping explains the maximum amount of variance in the data. This procedure increases the spectral discrimination ability among terrestrial materials.

The first step was to stack the transformed images acquired after applying band rationing and the Euclidean distance algorithm to the TM Landsat images into one multi-band data set for each individual temporal TM mosaic (1985, 1990, 2000-2001). Then the PCA method was used to decorrelate the stacked data sets and to remove redundancy from the analyzed data set before applying automatic classification.

5.1.4. Landsat MSS enhancement

The MSS data were used only to delineate the water network, as the number of bands is limited to 4 (G, R and 2 near infrared bands). The PCA transformation using the original MSS data as input was applied before automatic classification.

5.1.5. Landsat image automatic classification

To classify land cover, unsupervised classification was used to automatically group pixels of PCA data sets into clusters of similar DN values, using a standard statistical approach, without requesting any pre-defined classes. The ISODATA (Iterative Self-Organising Data Analysis Technique) (Tou and Gonzalez, 1974) clustering method was employed. This method uses spectral distances in an iterative process to assign the pixels to classes, until spectral distance patterns on the image gradually emerge.

More classes than those of interest are requested by the classifier to achieve a detailed identification of the data variation; thus 25 initial classes were set, and these classes were adjusted to 9 after the classification (**Plate 7, page …**).

5.2. ASTER TIR data analysis

At-surface radiance was then used in three ways to extract information that could be related to the composition of the surface materials: i) a decorrelation stretch (DCS) (Gillespie *et al.,* 1986), ii) calculation of the emissivity spectra using the alpha residual spectra (Kealy and Hook, 1993), iii) calculation of the TIR mineralogical ratios.

5.2.1. Decorrelation stretch (DCS)

The first step in the analysis was evaluation of the ASTER TIR data to discriminate the compositional properties of the Sechura desert surface using a decorrelation stretching (DCS) technique. The DCS is a transformation of the original data that removes the high correlation commonly found in TIR multispectral data sets and allows thermal and emissivity variations to be distinguished visually (Gillespie *et al.*, 1986). In this way, decorrelation stretching subdues correlated radiance variations due to scene temperatures and exaggerates spectral differences. The summarized results in **Plate 4a, page …** exhibit variations in the mineral composition of the surface using the combination of the TIR channels 14 (R), 12 (G) and 10 (B) that have been found to be particularly effective for ASTER TIR data (Rowan & Mars, 2003).

5.2.2. Alpha-derived emissivity (ADE)

Secondly, Alpha Residuals were used to produce alpha residual spectra that approximate the shape of emissivity spectra from TIR data. The Alpha-derived emissivity (ADE) method was developed by Kealy and Gabell (1990) and Hook *et al.* (1992). The approach utilizes Wien's approximationof the Planck function so it makes possible to linearize the approximation with the logarithmus given by Kealy and Hook (1993). The temperature and emissivity terms are separated and means are used to subtract the temperature term out. The alpha residual spectra are a function of emissivity (ϵ) only and preserve the shape of emissivity spectra but have a zero mean. As result, the alpha residuals method produces images with alpha values for every channel instead of actual emissivity value and doesn't provide a temperature image.

5.2.3. TIR mineralogical ratios

The alpha-derrived emissivity bands calculated from ASTER TIR radiance data using the above-mentioned method were further utilized. Several mineralogical indices were used to detect mineralogical compositions of quartz-rich, carbonate-rich and gypsum-rich lithologies.

Quartz and unaltered rocks composed of silicate minerals typically do not exhibit any spectral features in VNIR and SWIR. In contrast, they have prominent spectral features in the TIR region due to fundamental asymmetric Si-O-Si stretching vibrations. Quartz exhibits absorption features (e. g., emissivity minima) in ASTER bands 10 and 12, and higher emissivity in bands 11, 13 and 14 (Ninomia *et al.*, 2005). From the spectral emissivity property of quartz described above, the quartz rich lithologies can be enhanced using the following ratio:

$$QI = B_{13}/B_{10} \text{ (Hewson et al., 2005)}$$

Major *carbonate* minerals show spectral emissivity minima in ASTER band 14 (near 11.4 μm for calcite and 11.2 μm for dolomite) due to the C-O bending mode (Ninomia et al., 2005). Based on this finding, the Carbonate Index (CI) can be calculated from ASTER TIR data:

$$CI = B_{13}/B_{14} \text{ (Ninomia and Fu, 2002)}$$

Additionally, some sulfate minerals including *gypsum* have a very strong absorption in band 11 (near 8.7 μm) due to stretching fundamentals. As a result, they exhibit lower emissivity in band 11 than in bands 10 and 12 (Ninomia *et al.*, 2005). In our study, a simple band ratio was calculated in order to enhance the sediments enriched in gypsum:

$$GyI = B_{12}/B_{11}$$

5.3. Definition of land-cover classes

In situ detailed investigations, together with the synoptic analysis of the Landsat (e.g., mineral composition) and ASTER TIR scenes (e.g., decorrelation stretch, alpha-derived emissivity, TIR mineralogical ratios), formed the basis for definition of the land cover classes used in our study. In addition, XRD analysis together with spectral reflectance measurements (Chapter 3 and **Figure 1**) were conducted on 18 samples collected in the field to resolve the mineralogical composition (**Plate 3 and 4, pages … and …**). It was found that the sedimentary types mainly differ in the distribution of calcite, clay and gypsum and thus the abundance of these minerals in the collected samples was studied in detail (**Plate 4, page …**). As result, nine land-cover classes were defined; these were assumed to represent major surface materials (**Plate 6, page …**) detectable by Landsat/ASTER TIR data in the study area (**Plate 7, page …**):

- *Water network / water bodies:* These are represented by fluvial channels, permanent and ephemeral lakes.

- *Irrigation channels:* additionally, rice fields could also be classified as water bodies during the initial phase of cultivation.

- *Vegetation* can be mostly found in the floodplain areas of the Chira and Piura rivers as a result of agricultural activities. The desert in itself has a relatively flat, mostly vegetation-free surface, or exhibits distinct associations of vegetation types (e.g., ancient aeolian deposits).

- *Non-active surfaces* consist of two different lithological groups:

  – *Bedrock* is a class that includes magmatic and metamorphic rocks of crystalline massifs: Mesozoic and Cenozoic sediments of Talara and Sechura forarc basins characterized by alternations of sandstones, siltstones and claystones which are centimeters to decimeters thick. This class is exposed in the areas affected by intensive erosion (e.g., Bayovar and Paita areas, badland north of San Jacinto, **Plate 1, page …**).

  – *Ancient (non-active) aeolian deposits:* These are characterized by fine-grained siliciclastics; unlike the young aeolian sediments (described below) they contain greater admixtures of silt and clay. These deposits form the local elevation east of the city of Piura and are covered by sparse vegetation. Furthermore, these deposits are not affected by erosion.

- *Coarse-grained bioclastics***:** These outcrops mostly represent shoal marine deposits (called "Tablazos") and are generally composed of thick-bedded coarse-grained bioclastic limestones with variations in admixtures of siliciclastic material. The shoal marine deposits are mostly a few meters thick, reaching a maximum of 20 meters.

- *Siliciclastics:* These are characterized by young alluvial and aeolian deposits. Alluvial accumulations are represented by channel fills of braided ephemeral streams and by alluvial fans. Aeolian accumulations create dune fields that are elongated according to wind direction. They form belts up to 30 km long and up 1.5 km wide. Barchans dominate in these dune fields. Outside of the dune fields, aeolian material accumulates as thin sheets. These accumulations are only a few centimeters thick.

- *Siliciclastics with admixtures of clay minerals:* This material represents a mixture of aeolian silica-rich material and the other rocks (e. g., bedrock, bioclastics, alluvial sediments and the ancient, non-active aeolian deposits).

- *Evaporites (mainly gypsum):* Represent deposits accumulated in areas of ephemeral lakes as result of water evaporation.

- *Evaporites with admixtures of aeolian deposits:* These are the mixing material between aeolian deposits and evaporites.

6. RESULTS AND DISCUSSION

The present analysis indicates three significant effects of climatic changes on surface evolution: i) changes in extent of aeolian deposits, ii) changes in the pattern of fluvial channels, iii) changes in the extent of ephemeral lakes and their deposits. These findings describe well the spatial-temporal dynamics of the Sechura desert system and are in accordance with other studies performed in desert environments (Katra and Lancaster, 2008). An episodic influx of surface water introduces clastic material to the ephemeral lakes, while evaporation of subsurface brines leads to accumulation of chemical constituents on and within the subsurface (Rosen, 1994). The sedimentation processes in ephemeral lakes result in dynamic surfaces that are then vulnerable to wind erosion and become productive areas for aeolian dust. Desert dust has then many impacts on the climate, ecosystems and also humans (Goudie and Middleton, 2006).

It is also important to discuss issues related to data quality and stability, as the multitemporal images form different sensors were processed to detect changes in the study area. In our study, atmospheric correction was applied to ASTER TIR data only, although variation in phenology and detector performance between Landsat 5 and 7 was reported (Teillet *et al.*, 2000). However, this effect, which can introduce discrepancies into the final interpretation, was minimized by the two-step image transformation (band ratios and PCA transformation) applied before the automatic classification, thus the absolute DN values were not used to classify the images.

The final change detection is discussed on the classified images; furthermore, two after-event images, although they represent the data acquired by two different Landsat sensors (Landsat 5 scenes from 1985 and Landsat 7 scenes from 2000-2001), they both show consistent results that illustrate the dynamic processes in the dessert environment.

The more precise change detection focusing on the pre-processing techniques (e.g., sensor calibration and atmospheric correction) is planned in a future

study. This analysis will be applied to extensive time-series Landsat images, as all the Landsat archive scenes have been available for free since the end of 2008. Additionally, classification of the ASTER VNIR and SWIR bands will be also employed to facilitate detailed mineral discrimination.

6.1. Landsat and ASTER image analysis

The mineralogical composition of the sediments is primary a determinant of their inherent reflectance properties. The XRD analysis together with spectral reflectance measurements conducted on the sediment samples (chapter 3 and **Figure 1**) helped to explain the colour tones in **Plate 3, page …** that displays the RGB colour composition of the mineral indices (R: 5/7, G: 5/4, B: 3/1) calculated from 1985, 1990 and 2000/2001 temporal TM mosaics.

The aeolian high-quartz material is rich in goethite, therefore displays in tones of blue. Yellowish colour (mixing result between R: 5/7 and G: 5/4) corresponds to calcite-rich lithologies bearing also ferroan (e.g., coarse-grained bioclastics) and is a result of calcite absorption detected by TM7 band (bright pixels in 5/7 ratio image) and ferroan absorption detected by TM4 (bright pixels in 5/4 ratio image). Red, in our case, mostly corresponds to vegetated agricultural land, as steep slope between high TM5 values and low TM7 values of a vegetation spectral curve (**Figure 1**) results in high 5/7 ratio values. Greenish tones correspond to the "older" lithologies (crystalline bedrock). They represent the rocks containing Fe-bearing aluminosicates (e.g., phyllite and gneiss) and in the 5/4 ratio image appear as very bright pixels. Very light mixing colours between blue/red and blue/green are then assumed to show mixing material between aeolian sediments and the underlying and/or surrounding geological material (e. g., siliciclastics with admixture of clay minerals). Evaporites display as magenta (high values in B: 3/1and R: 5/7) and the mixing material between evaporites and aeolian sediments appears in tones of pink to light purple in colour.

The differences in extent of the aeolian sediments in the Landsat scene acquired during a dry (between-El Niño) period (1990) and the other one acquired after El Niño events (1985 and 2000/2001) are quite visible, as a blue colour corresponding to silica-rich aeolian deposits dominates in the dry-period scene from 1990. On the other hand much fewer green parts are visible and the yellow colour has almost disappeared in the image from 1990. Both after-event images (1985 and 2000/2001) then show comparable colour patterns, as the aeolian deposits have smaller extent and bigger parts of the older lithologies are exposed in both images. The extent of the evaporites is greater in the after-event images as they are the products of water evaporation. The mixing materials between evaporites and aeolian sediments remain more or less the same. This shows that the soil in the areas surrounding the lakes is persistently saline.

The changes in vegetation and agriculture, respectively, are also quite significant and indicate that agricultural activities have been rather extensive along the Piura and Chira rivers during the last three decades. The final classifications of the Landsat images from 1985, 1990 and 2000/2001 (**Plate 7, page …**) reflect the mineral differences enhanced by calculating mineral indices (**Plate 3, page …**).

Plate 4, page … displays the results of ASTER TIR analysis. In all the three images, silica-rich material is displayed in tones of red, calcite-rich material in tones of blue and evaporites in tones of green. Comparing the three methods (alpha-emissivity, decorrelation stretch, TIR mineralogical ratios, **Plate 4c, page …**), decorrelation stretch and TIR mineralogical ratios yield similar information. The least clear image in terms of mineralogical content was achieved by displaying alpha-emissivity bands without employing any additional enhancement technique. The ratio method seems to be most efficient of all of the three described methods, as the information is more consistent between the two temporal mosaics (2006 and 2007) and it defines the mineralogical content in the clearest way.

The TIR ratio image (R: QI, Quartz Index; G: GyI, Gypsum Index; B: CI, Carbonate Index) allowed us to identify the quartz-rich lithologies, carbonates (blue) end evaporites (green) very well. Following the colour scheme in **Plate 4c, page …**, the area between the ephemeral lakes (e.g., La Niña, S. Ramon, Ñapique) and the shoreline can be described as carbonates covered to some extent by aeolian silica-rich sediments and by a mixture of aeolian deposits and evaporites. This is in accordance with the geological situation found in the field. However, as TM7 band covers carbonate as well as clay mineral absorptions, analysing Landsat images we were able to classify this area only as aeolian and aeolian deposits mixing with clays and evaporites, respectively.

6.2. Changes between 1973-2001 in the study area

6.2.1. Chira and Piura catchments

Changes in the geometry and position of the Chira and Piura channels are the most significant indications of high discharges during the ENSO

events. The Landsat MMS scene from 1973 had thick cloudiness covering the whole Chira catchment; therefore it was possible to construct the Chira fluvial system only for 1984, 1990 and 2000/2001. The biggest difference in the Chira river network can be seen between a low discharge year 1990 (**Plate 8, page …**) and high discharge years 1984 and 2000/2001 (**Plate 8, page …**). We assume that the ancient/abandoned river channels are reactivated during El Niño events. The high discharge years, 1984 and 2000/2001, exhibit very similar river network geometry patterns. The differences in the positions of low and high discharge river channels are in the range of hundreds meters but can reach a maximum of several kilometres.

The fluvial fan of the Piura River is a sedimentary system where such changes as bifurcations and avulsions are typical processes of channels evolution. Based on a channel pattern, this sedimentary system could be interpreted as a fluvial system with short-lived anastomosis (Rajchl *et al., 2008*), where an anastomosing network of channels is established during high discharge episodes, commonly by formation of crevasse splays and reoccupation of older channels. The best example demonstrating temporal reactivation of the abandoned channels can be seen in 1984 (**Plate 8, page …**), when the old channel, which had not been used at least since the El Niño event in 1926, was temporally activated again. The reconstruction of the fluvial system from a dry period scene (1990) was the most problematic, as the major river channel transported much less water at that time and it was difficult to differenitate between the main river channels and artificial irrigation channels.

However, other big differences in the Piura channel network were detected for the years 1990 and 2000. The analysis shows that the principal channel of the Piura River moved several kilometres eastward in that decade (**Plate 8, page …**). Although this could be partially explained by autocyclic evolution of the system associated with vertical aggradation of the fluvial ridge (Mackey & Bridge, 1995), tectonic tilting of the sedimentary surface caused by subsidence on normal fault(s) merging the Sechura Basin from the east could be also speculated (Bridge & Mackey, 1993; Peakall *et al.*, 2000).

During floods (**Plate 8, page …**, situation from 1973, 1984, 2000), an extensive lacustrine system forms in zone of endorheic depressions (**Plate 8, page …**). Later, a majority of the originally flooded area is covered by salt accumulation as the lacustrine water evaporates (compare **Plate, 3, 4 and 8, pages …, … and …**). The lacustrine system is also affected by seasonal water table changes between dry and wet periods. In **Plate 5, page …**, the lakes are flooded at the end of the wet season (05/2006); however they became completely dry within 7 months (01/2007). The previously flooded area is already covered by newly created evaporites.

6.2.2. The ENSO sediment dynamics

The final classified results of the Landsat TM data (**Plate 7, page …**) prove the findings described above and allow us to state that, during the El Niño cycle, significant changes occur in the extent, not only of the evaporites, but also of the aeolian material. During the high discharge period, an extreme amount of water and sedimentary material is brought to the lower catchments of the Chira and Piura rivers and consequently to the ephemeral lakes. In the area of ephemeral lakes, the aeolian accumulations are partially eroded and redistributed by water flows during the floods. Outside of the flooded zones, sheet erosion, which is the effect of unconfined flows of water running across the surface, causes denudation of aeolian material.

After the high discharge period, the evaporation in the flooded areas allow rapid formation of new evaporite sediments and wind transport of sandy material increases. As result, new aeolian material covers the older formations and, within short time, also the newly formed evaporites. This process continues until a new El Niño event again brings enormous amounts of water and material, exposes the older formations and facilitates new evaporite formation.

7. CONCLUSIONS

The ENSO phenomenon strongly affects the environment in the northwestern part of Peru. The approach employed here, involving a uniform classification technique applied to Landsat time-series data and mineral mapping technique applied to ASTER TIR data, has shown that the fluvial system and major surface sediments can be identified; furthermore, the changes in the landscape occurring after and between the catastrophic events can be defined by analysing time-series data. The ASTER TIR mineralogical ratios (QI, GyI, CI) allowed identification of quartz-rich, gypsum-rich and carbonate-rich sediments.

The classification technique combining the Landsat TM band rationing method with a texture-enhancing algorithm (Euclidean distance) enabled delineation of fluvial systems and water bodies. Furthermore, using this technique we were able to classify surface materials as evaporites, siliciclastics, bioclastics, non-active surface (e.g., crystalline bedrock, ancient aeolian sediments), aeolien material, and aeolien material which is present in mixtures with other sediments.

Reconstruction of the fluvial systems of the Chira and Piura rivers shows that both rivers can dramatically change their channel geometry and position by reactivating their ancient/abandoned channels during floods. The analysis has also demonstrated that high and low discharge periods significantly affect not only the water table and consequent evaporite evolution, but also the spatial extent of the aeolian deposits. During the high discharge period, the older rocks are exposed to a larger extent and evaporite crusts are created in the previously flooded areas due to the very rapid evaporation. The sedimentation processes in ephemeral lakes result in dynamic surfaces that are prone to wind erosion and, consequently, during the dry period the aeolian sediments again cover large areas due to wind transport carrying the material that was previously transported by the fluvial system to the ephemeral lakes during the floods. All the selected techniques can be employed using standard, either free or low-cost satellite images (e.g. Landsat, ASTER).

8. ACKNOWLEDGEMENTS

The present research was undertaken within a framework of the Czech-Peruvian international cooperation project "Research and evaluation of geomorphological and hydrogeological conditions of the Piura River basin to mitigate environmental factors restricting social and economic progress of the region", funded by the Czech Ministry of the Environment and the Ministry of Foreign Affairs (Grant No. RP/5/2007). The authors are grateful to the Regional Government in Piura for their support and collaboration on this project.

9. BIBLIOGRAPHIE

ABRAMS, J.- M., 1983. Remote sensing for porphyry copper deposits in Southern Arizona. *Economic Geology*, **78**, pp. 591-604.

ABRAMS, M., 2000. The Advanced Spaceborne Thermal Emission and Reflection Radiometer (ASTER): data products for the high spatial resolution imager on NASA's Terra platform. *International Journal of Remote Sensing,* **21,** 847–849.

ACEITUNO, P., 1987. On the lnterannual variability of South American climate and the Southern Oscillation. Thesis Univ. Wisconsin, Madison, 128 pp.

ACEITUNO, P, 1988. On the functioning of the Southern Oscillation in the South American sector Part 1 *Surface climate Mon Weather Rev*, **116**, 505-524.

BARNETT, T.- P., 1981 Statistical relations between ocean/atmosphere fluctuations in the Tropical Pacific. *J Phys Oceanogr*, **11**, 1043-1058.

BASSANI, C., CAVALLI, R. - M., PALOMBO, A., PIGNATTI, S., & MADONNA, F., 2006. Laboratory activity for a new procedure of MIVIS calibration and relative validation with test data. *Annals of Geophysics*, **49**(1), 45-56.

BASTIAANSSEN, W.-G.-M., 1998. Remote Sensing in Water Resources Management. In *The state of the art International Water Management Institute*, Colombo, Sri-Lanka, 118 p.

BERBEROGLU, S.- A., AKIN, A., 2009. Assessing different remote sensing techniques to detect land use/cover changes in the eastern Mediterranean. *International Journal of Applied Earth Observation and Geoinformation*. **11**, 46–53.

BISHOP, J.- L., MURAD, E., 1996. Schwertmannite on Mars? Spectroscopic analyses of schwertmannite, its relationship to other ferric minerals, and its possible presence in the surface material on Mars. In M.D. Dyar, C. McCammon, and M.W. Schaefer, Eds., Mineral Spectroscopy: A Tribute to Roger G. Burns, Special Publication n° 5, *The Geochemical Society*, Houston, Texas, p. 337–358.

BRIDGE, J.-S., MACKEY, S.-D., 1993. Revised alluvial stratigraphy model. In: MARZO, M., PUIGDEFÁBREGAS, C. (Eds.) *Alluvial Sedimentation. IAS Spec. Publ.* 17, Blackwell, Oxford, p. 319-336.

CALDAS, J., PALACIOS O., PECHO, O., VELA, C., 2000. Geologia de los cuadrangulos de: Bayovar, Sechura, La Redonda, Pta. La Negra, Lobos de Tierra, Las Salinas y Morrope. Hojas 12a - 12b - 12c - 13a - 13b - 13c - 14c. Boletin n° 32, Série A. *Carta Geológica Nacional*, **78** p., INGEMMET, Lima.

CAVIEDES, C.-N., 1973. Secas and E1 Niño. Two simultaneous climatical hazards in South America. Proc Assoc Am Geogr, **5**, 44-49.

CAVIEDES, C.-N., 1975. El Niño 1972, its climatic ecological,human and economic implications. *Geogr Rev*, **65**, 494-509.

CAVIEDES, C.-N., 1984. El Niño 1982-83, *Geogr Rev*, **74**, 267-290.

DEWIDAR, K.-H.-M., & FRIHY, O.-E., 2003. Thematic Mapper analysis to identify geomorphologic and sediment texture of El-Tineh plain, north-western coast of Sinai, Egypt. *International Journal of Remote Sensing*, **24**, 2377–2385.

DEWIDAR, K.-H.-M., 2000. Landfilling detection of Hurghada, North Red Sea, Egypt, by using Thematic Mapper. *International Journal of Remote Sensing*, **23**,939–948.

DEWIDAR, K.-H.-M., 2004. Detection of the land use/land cover changes for the northern part of the Nile delta (Burullus region), Egypt. *International Journal of Remote Sensing*, **25**(20), 4079–4089.

EKLUNDH, L., SINGH, A., 1993. A comparative analysis of standardized and unstandardized princi-

pal components analysis in remote sensing. *International Journal of Remote Sensing*, **14**, 1359-1370.

FRANCOU, B., PIZARRO, L., 1985. E1 Niño y la sequía en los altos Andes Centrales (Perú y Bolivia), *Bull Inst Fr Estud Andines*, Lima, 14, 1-18.

GILLESPIE, A.-R., KAHLE, A.-B., WALKER, R.-E., 1986. Color enhancement of highly correlated images: I. Decorrelation and HIS contrast stretches. *Remote Sensing of Environment,* **20**, 209-235.

GILLESPIE, A., COTHERN, J.- S., ROKUGAWA, S., MATSUNAGA, T., HOOK, S.- J., KAHLE, A.- B., (1998). A temperature and emissivity separation algorithm for Advanced Spaceborne Thermal Emission and Reflection Radiometer (ASTER) images. *IEEE Transactions on Geoscience and Remote Sensing*, **36(4)**, 1113–1126.

HASTENRATH, S., HELLER, L., 1977. Dynamics of climatic hazards in northeast Brazil, *Q J R Meteorol Soc*, **10**, 77-92.

GOUDIE, A.-S., MIDDLETON, N.- J., 2006. Desert dust in the global system. NY: Springer.

HEWSON, R.-D., CUDAHY, T.-J., MIZUHIKO, S., UEDA, K., MAUGER A.-J., 2005. Seamless geological map generation using ASTER in the Broken Hill-Curnamona province of Australia, *Remote Sensing of Environment* **99**, 159-172.

HOOK, S.-J., GABELL, A.-R., GREEN, A.-A., & KEALY, P.-S., 1992. A comparison of techniques for extracting emissivity information from thermal infrared data for geologic studies. *Remote Sensing of Environment*, **42**, 123-135.

HOREL, J.-D., WALLACE, J.-M., 1981. Planetary-scale atmospheric phenomena associated with the Southern Oscillation Mon Weather Rev, **109**, 813-829.

IRON, J.-R., PETERSEN G.-W., 1981. Texture Transforms of Remote Sensing Data. Remote Sensing of Environment, **11,** 359-370.

JOHNSON, B.-R., 1998, In-scene Atmospheric Compensation: Application to SEBASS Data Collected at the ARM Site. Part I Technical Report, Space and Environment Technology Center, The Aerospace Corporation.

KATRA, I., LANCASTER, N., 2008. Surface-sediment dynamics in a dust source from spaceborne multispectral thermal infrared data, *Remote Sensing of Environment*, **112**, 3212–3221.

KEALY P.-S., GABELL, A.-R., 1990. "Estimation of emissivity and temperature using alpha coefficients," in Proc. *2nd TIMS Workshop. Pasadena, CA: Jet Propul. Lab., JPL Publication*, 90-55.

KEALY, P.-S., HOOK, S.-J., 1993. Separating temperature and emissivity in thermal infrared multispectral scanner data: Implications for recovery of land surface temperatures, *IEEE Transactions on Geoscience and Remote Sensing*, **31**, 1155-1164.

KILADIS, G.- N., DIAZ, H.- F., 1989. Global climatic anomalies associated with extremes in the Southern Oscillation, *J Climate*, **2**, 1069-1090.

KIRKLAND, L., KENNETH, H., KEIM, E., ADAMS, P., SALISBURY, J., HACKWELL, J., 2002. First use of an airborne thermal infrared hyperspectral scanner for compositional mapping, *Remote Sensing of Environment*, **80**, 447-459.

LIBERTI, M., SIMONIELLO, T., CARONE, M.T., COPPOLA, R., D'EMILIO, M., MACCHIATO, M., 2009. Mapping badland areas using LANDSAT TM/ETM satellite imagery and morphological data, *Geomorphology*, **106**, 333-343.

LOURENS, U., 1990. Using Landsat TM to monitor irrigated land at the individual farm level. In: Menenti, M. (Ed.), In *Remote Sensing in Evaluation and Management of Irrigation*. Instituto Nacional del Ciencia y Tecnicas Hidricas, Mendoza, Argentina, pp. 231-235.

NINOMIYA,Y., FU, B.,CUDAHY, J., 2005. Detecting lithology with Advanced Spaceborne Thermal Emission and Reflection Radiometer (ASTER) multispectral thermal infrared ''radiance-at-sensor'' data, *Remote Sensing of Environment,* **99,** 127-139.

NINOMIYA, Y., FU, B., 2002. Quartz index, carbonate index and SiO2 content index defined for ASTER TIR data, *Journal of Remote Sensing Society of Japan*, **22**, 50-61.

QUINN, W.- H., NEAL, V.- T., 1992. The historical record of El Niño events. In RS Bradley and PD Jones (Editors), *Climate since AD 1500,* Routledge, London, 623-648 pp.

PALACIOS, O., 1994. Geologia de los cuadrangulos de: Paita, Piura, Talara, Sullana, Lobitos, Quebrada Seca, Zorritos, Tumbes y Zarumilla. Hojas 11-a, 11-b, 10-a, 10-b, 9-a, 9-b, 8- b, 8-c y 7-c. Boletin No. 54, Série A. *Carta Geológica Nacional*, INGEMMET, Lima, 190 p.

PEAKALL, J., LEEDER, M., BEST, J., ASHWORTH, P., 2000. River response to lateral ground tilting: a synthesis and some implications for the modelling of aluvial architecture in extensional basins. Basin Research, **12**, p. 413-424.

RAJCHL, M., NÝVLT, D., KOPAČKOVÁ, V., EBESTA, J., VÍT, J., HROCH, T., 2008. Geomorphological evolution of the Piura river fluvial fan, Northern Peru, preliminary study, In *Abstract Volume of XIII Latin-American Geological Congress*, XIV Peruvian Geological Congress, Pontifical Catholic University of Peru, Lima Peru.

RASMUSSON, E., M., 1985. E1 Niño and varriations in climate, *Atm Sci*, **73**, 168-177.

REIN, B., 2007. How do the 1982/83 and 1997/98 El Niños rank in a geological record from Peru?, *Quaternary International*, **161**, 56–66.

ROGERS, J.- C. 1988. Precipitation variability over the Caribbean and tropical Americas associated with the Southern Oscillation, *J Climate*, **1**, 172-192.

ROPELEWSKI, C.- F., HALPERT, M.- S., 1987. Global and regional scale precipitation patterns associated with El Niño/Southern Oscilation, *Mon Weather Rev*, **115**, 1606-1626.

ROSEN, M.- R., (1994). The importance of groundwater in playas: A review of playa classifications and the sedimentology and hydrology of playas. In M. R. Rosen (Ed.), Paleoclimate and basin evolution of playa systems: *Geological Society of America Special Paper*. **289**., pp. 1-18.

ROWAN, L.- C., MARS, J.- C., 2003. Lithologic mapping in the Mountain Pass, California area using Advanced Spaceborne Thermal Emission and Reflection Radiometer (ASTER) data. *Remote Sensing of Environment*, **84**, 350-366.

SALZANO, R., SALVATORI, R., DOMINÉ, F., 2008. Investigation on the relation between physical and radiometrical properties of snow cover. *EARSeL eProceedings*. **7(2)**, ISSN 1729-3782.

SCHEIDT, S.,RAMSEY, M.,LANCASTER N., 2008. Radiometric normalization and image mosaic generation of ASTER thermal infrared data: An application to extensive sand sheets and dune fields. *Remote Sensing of Environment*, **112**, 920–33..

SMALL, C., STECKLER, M., SEEBER, L., AKHTER, S.-H., GOODBRED JR., S.,MIA, B., IMAM, B. (2009). Spectroscopy of sediments in the Ganges–Brahmaputra delta: Spectral effects of moisture, grain size and lithology, *Remote Sensing of Environment*, **113**, 342-361.

SULTAN, M., ARVIDSON, R.- E., STURCHIO, N.- C., GUINNES, E.- A., 1987. Lithologic mapping in arid regions with Landsat TM data: Meatiq dome, Egypt. *Geological Society of America Bulletin,* **99**, 748-762.

TEILLET, P.- M., G. FEDOSEJEVS, R.- R. IRISH, J.- L. BARKER, AND B.- L. MARKHAM, 2000. «Landsat-7 ETM+ and Landsat-5 TM Cross-Calibration»; *Proceedings of the Twenty-Second Canadian Symposium on Remote Sensing*, Victoria, B.C., pp. 207-216.

TOU, J., GONZALEZ, R., 1974. Pattern Recognition Principles. Addison-Wesley Publishing Company, Reading, Massachusetts, 377 p.

VAUGHAN, R.-G., WENDY, M.-C., TARANIK, J.-V., 2003. SEBASS hyperspectral thermal infrared data: Surface emissivity measurement and mineral mapping. *Remote Sensing of Environment*, **85**, 48-63.

VISSER, T.-N.-M., 1989. Appraisal of the Implementation of Water Allocation Policies. ICW (Instituute voor Cultuurtechnick en Waterhuishouding), Wageningen, The Netherlands, 54 p.

WAYLEN, P.- R AND CAVIEDES, C.- N, 1986. El Niño and annual floods on the north Peruvian littoral, *J. Hydrol*, **89**, 141- 156.

YOUNG, S.- J., 1998. In scene atmospheric compensation: Application to SEBASS data collected at the ARM Site. Part II. Aerospace Corporation technical report, ATR-99 (8407)-1.

DÉTECTION DES CHANGEMENTS INDUITS PAR EL NIÑO-OSCILLATION AUSTRALE À L'AIDE DE DONNÉES SATELLITAIRES MULTITEMPORELLES : EXEMPLE DU NORD-OUEST PEROU

Veronika KOPAČKOVÁ*[1], Michal RAJCHL[1], Jan HARBULA[1], František LAUFEK[1], Daniel NÝVLT[1], Tomáš HROCH[1], Hanuš JAN[1]

[1]Czech Geological Survey, Klárov 3, 118 21, Prague 1, Czech Republic
[2]Institute of Systems Biology and Ecology of the Academy of Sciences of the Czech Republic, Na Sádkách 7, České Budějovice, Czech Republic
*veronika.kopackova@seznam.cz; phone: +420/606 547 908; fax: 1 +420/257 531 376

RÉSUMÉ

Le désert de Sechura au nord du Pérou représente un système unique caractérisé par de très faibles précipitations. Les eaux de surface y sont concentrées suivant deux fleuves : le Chira et le Piura, qui drainent les eaux des Andes. L'apport d'eau dans ces deux rivières est contrôlé par les variations saisonnières (saison sèche et saison des pluies). Une fois tous les dix ans environ, ce système relativement stable est affecté par le fameux phénomène El Niño/oscillation australe (ENSO en anglais). Les conditions climatiques humides qui président normalement sur la zone ouest-pacifique migrent alors vers l'est où elles entraînent de très fortes précipitations qui ont pour conséquence d'apporter d'importantes quantités d'eau aux fleuves Chira et Piura. Les systèmes fluviatiles répondent à ces changements extrêmes par d'imprévisibles modifications de la géométrique de leurs chenaux. La présente étude couvre une surface totale de 20 000 km² et combine différentes techniques de cartographie à l'aide de données d'observation de la Terre : (a) scènes Landsat de 1973, 1984, 1985 et 2000-2001 ; (b) 6 scènes ASTER acquises en 2006-2007. Les scènes multitemporelles Landsat ont été interprétées pour reconstruire les réseaux fluviatiles du Chira et du Piura et classifier les dépôts de surface de l'environnement aride. L'analyse des canaux du domaine infrarouge thermique de ASTER a permis de dresser des cartes d'abondance en quartz, en carbonates et en gypse. Les résultats de l'étude des données multisources et multitemporelles fournissent une information essentielle sur l'évaluation des changements dans les parties inférieures des bassins du Chira et du Piura au cours des trois dernières décennies.

MOTS-CLÉS

Analyse multitemporelle, Rapport d'émissivité, occupation des sols, Désert de Sechura, Nord-Ouest Pérou, Landsat, ASTER TIR, ENSO.

LISTE DES TABLEAUX, FIGURES ET PLANCHES

Tableau 1 : *Réflectance (R) et émittance (E = 1 – R) de quelques minéraux (albite, microcline, calcite, quartz, muscovite, illite et montmorillonite) extraites à partir des courbes spectrales obtenues en laboratoire (sites web de l'USGS et du JPL), pour les bandes correspondant à ASTER.*

Figure

Figure 1 : *Spectres de réflectance de différents sédiments mesurés en laboratoire.*

Planches

Planche 1 : *Localisation géographique de la zone d'étude et de son environnement.*

Planche 2 : *Schéma du procédé d'analyse des données.*

Planche 3 : *Compositions colorées Landsat TM mettant en valeur les minéraux pour 1985 (A), 1990 (B) et 2000/2001 (C).*

Planche 4 : *Compositions colorées ASTER TIR : étalement avec décorrélation (A), émissivité (B), rapports de bandes ASTER montrant la minéralogie avec correction atmosphérique (C). La végétation est masquée (gris).*

Planche 5 : *Analyse des données ASTER TIR: rapports de bandes ASTER montrant la minéralogie pour mai 2006 – saison humide (A) et janvier 2007 – saison sèche (B). La végétation est masquée (gris).*

Planche 6 : *Photographies de terrain montrant les dépôts alluviaux de surface (A), roches silicoclastiques cénozoïques (B), le fleuve Chira (C, D), roches bioclastiques "Tablazos" (E, G), sédiments éoliens le long de l'océan (G), Evaporites – détail (H).*

Planche 7 : *Classification de l'occupation des sols à partir de Landsat TM pour 1985 (A), 1990 (B) et 2000/2001 (C).*

Planche 8 : *Modification dans la géométrie des chenaux de rivière et extension des lacs (1973-2000/2001).*

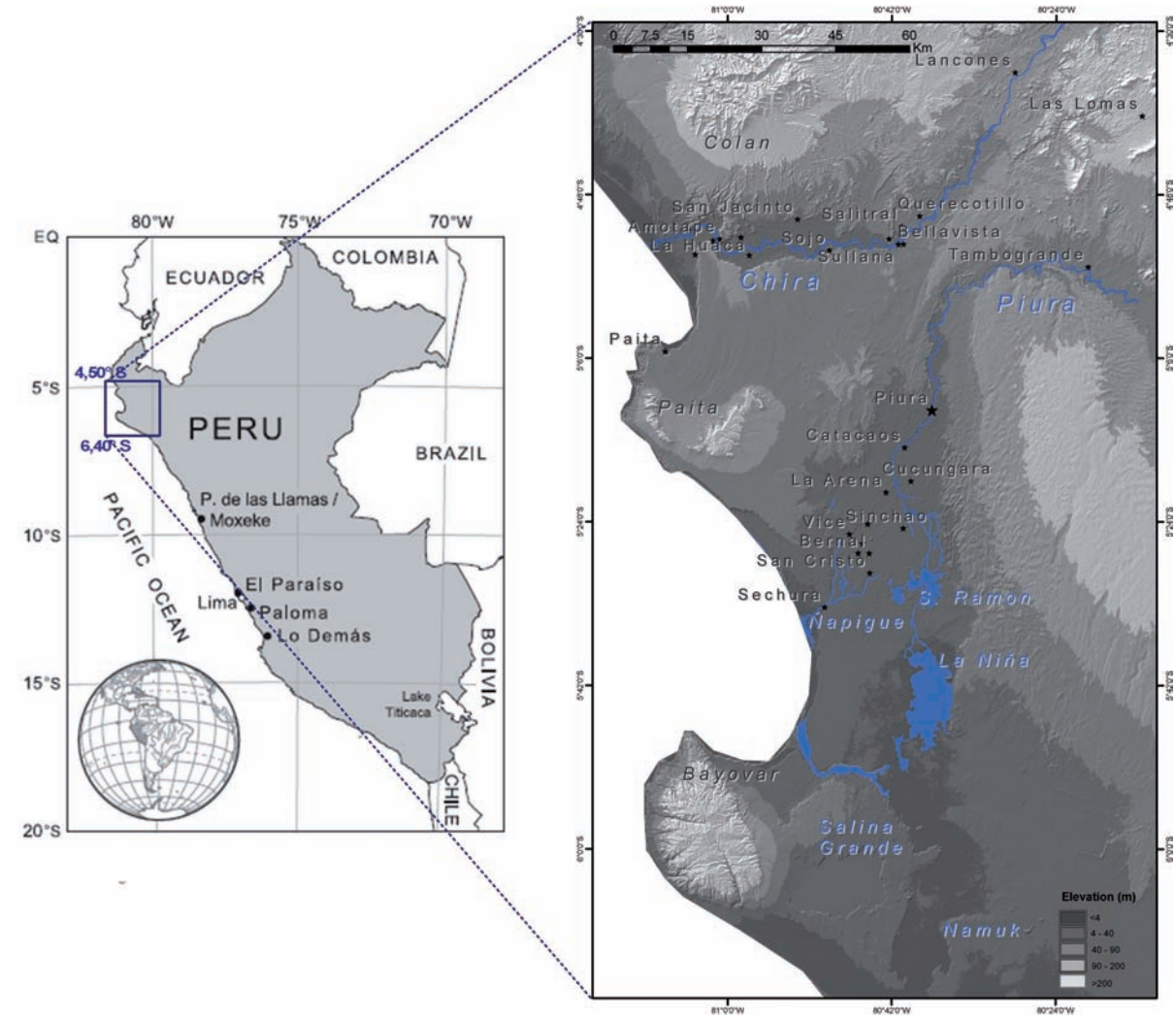

Plate 1: Geographic setting of the study area and its surrounding.

Planche 1 : *Localisation géographique de la zone d'étude et de son environnement.*

ARTICLE PAGE 64, V. KOPAČKOVÁ *et Coll.*

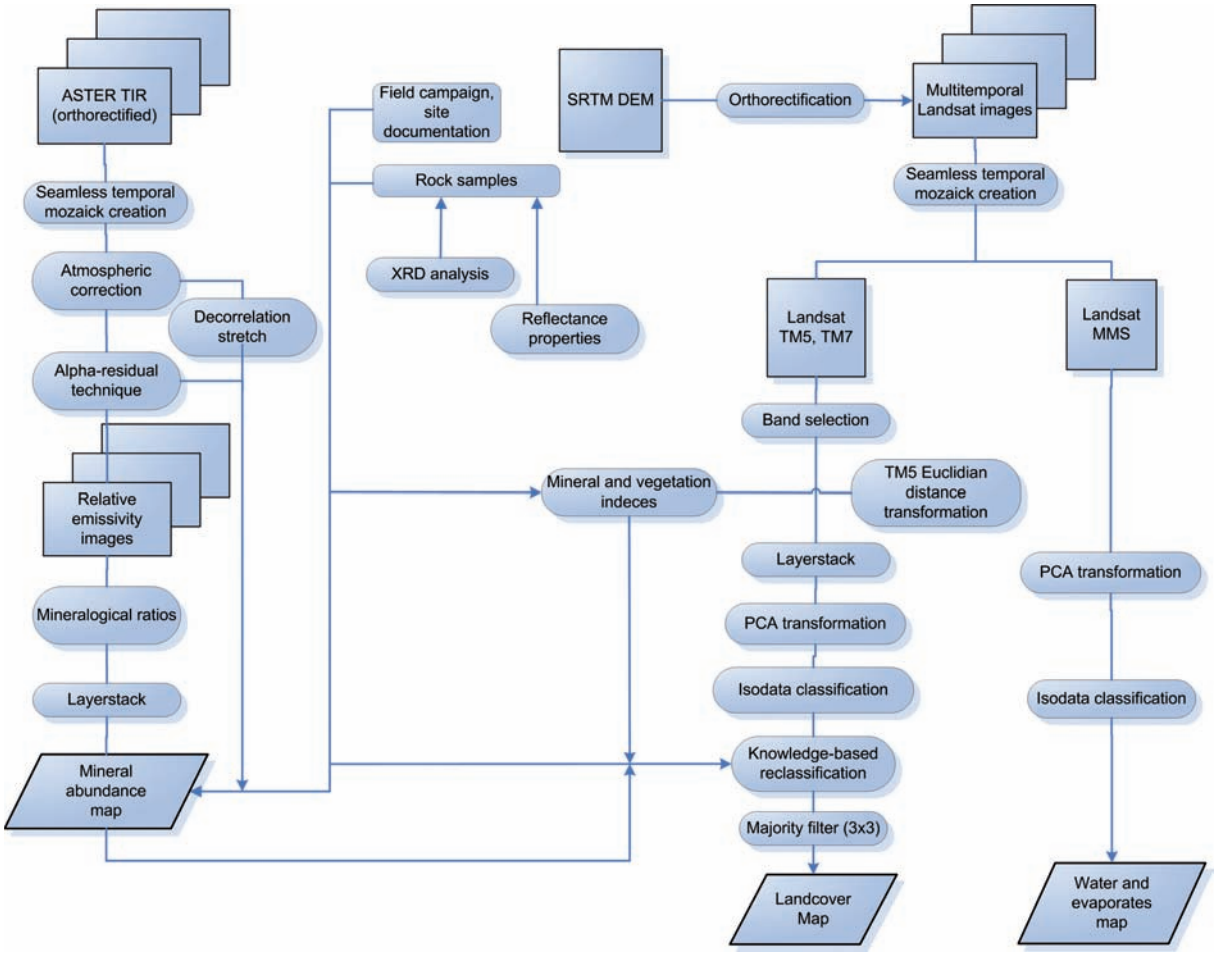

Plate 2: Flow chart documenting the data analysis process.
Planche 2 : *Schéma du procédé d'analyse des données.*

ARTICLE PAGE 64, V. KOPAČKOVÁ *et Coll.*

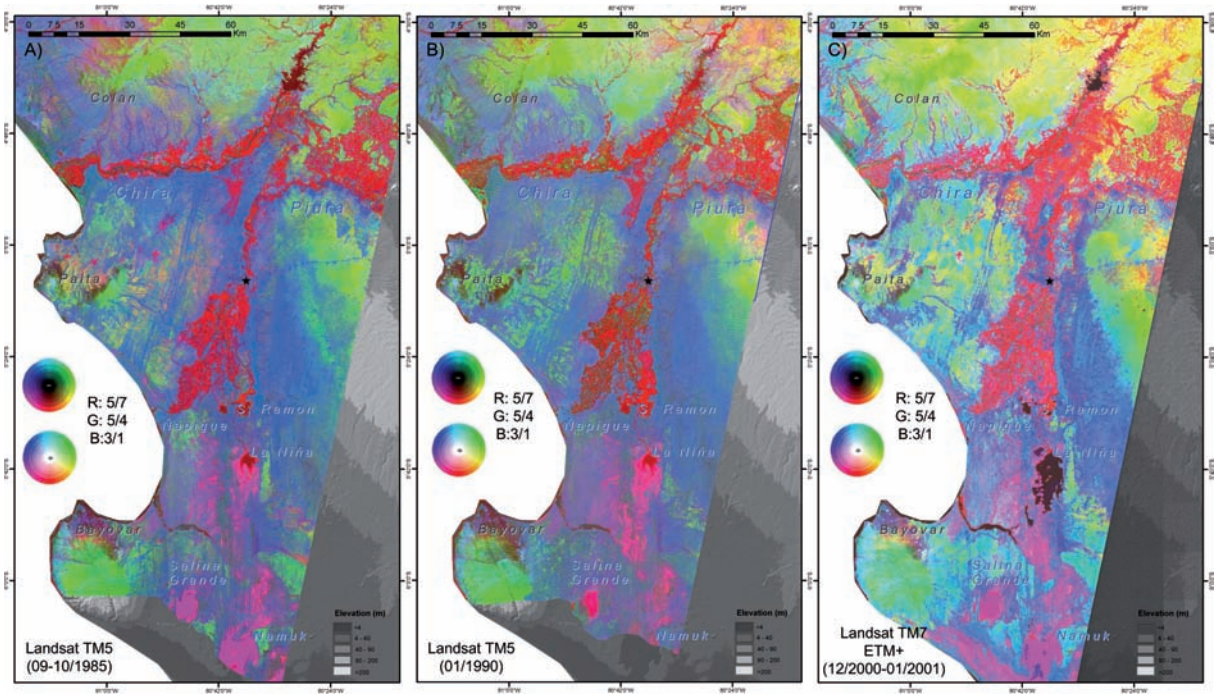

Plate 3: Mineral composition color scheme for Landsat TM images from 1985 (A), 1990 (B) and 2000/2001 (C).

Planche 3 : *Compositions colorées Landsat TM mettant en valeur les minéraux pour 1985 (A), 1990 (B) et 2000/2001 (C).*

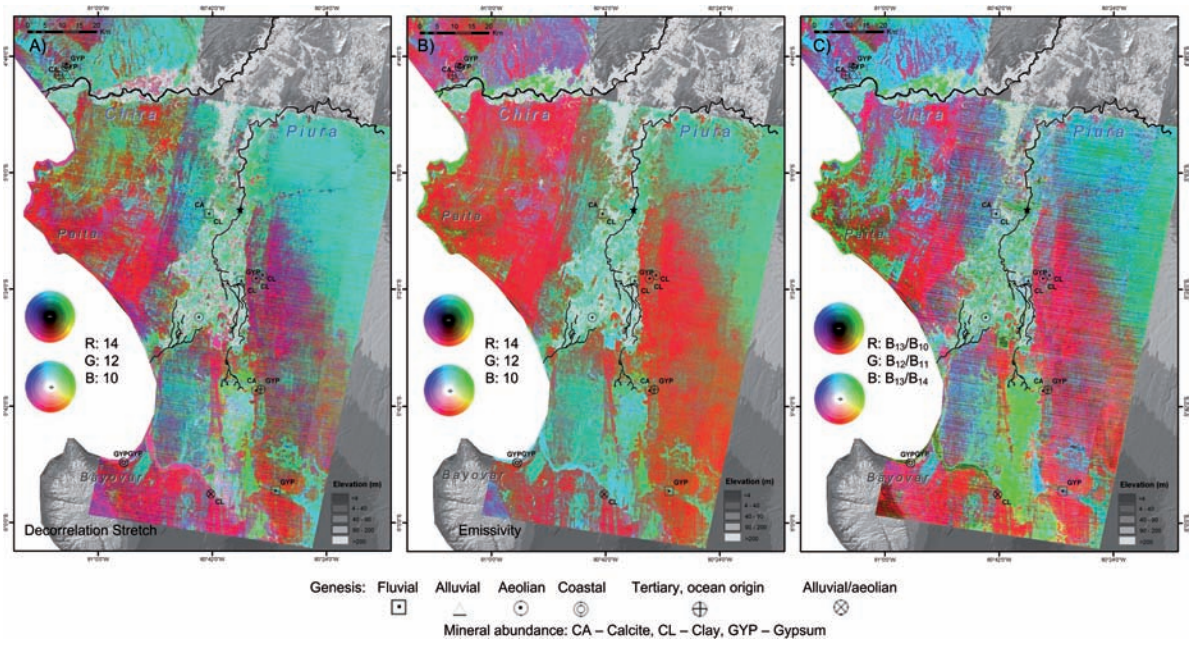

Plate 4: Aster TIR analysis RGB-color schemes: Decorrelation stretch (A), alpha-derived emissivity (B), mineralogical band ratios derived using the atmospherically corrected alpha residuals images (C). In grey is a vegetation mask.

Planche 4 : *Compositions colorées ASTER TIR : étalement avec décorrélation (A), émissivité (B), rapports de bandes ASTER montrant la minéralogie avec correction atmosphérique (C). La végétation est masquée (gris).*

ARTICLE PAGE 64, V. KOPAČKOVÁ *et Coll.*

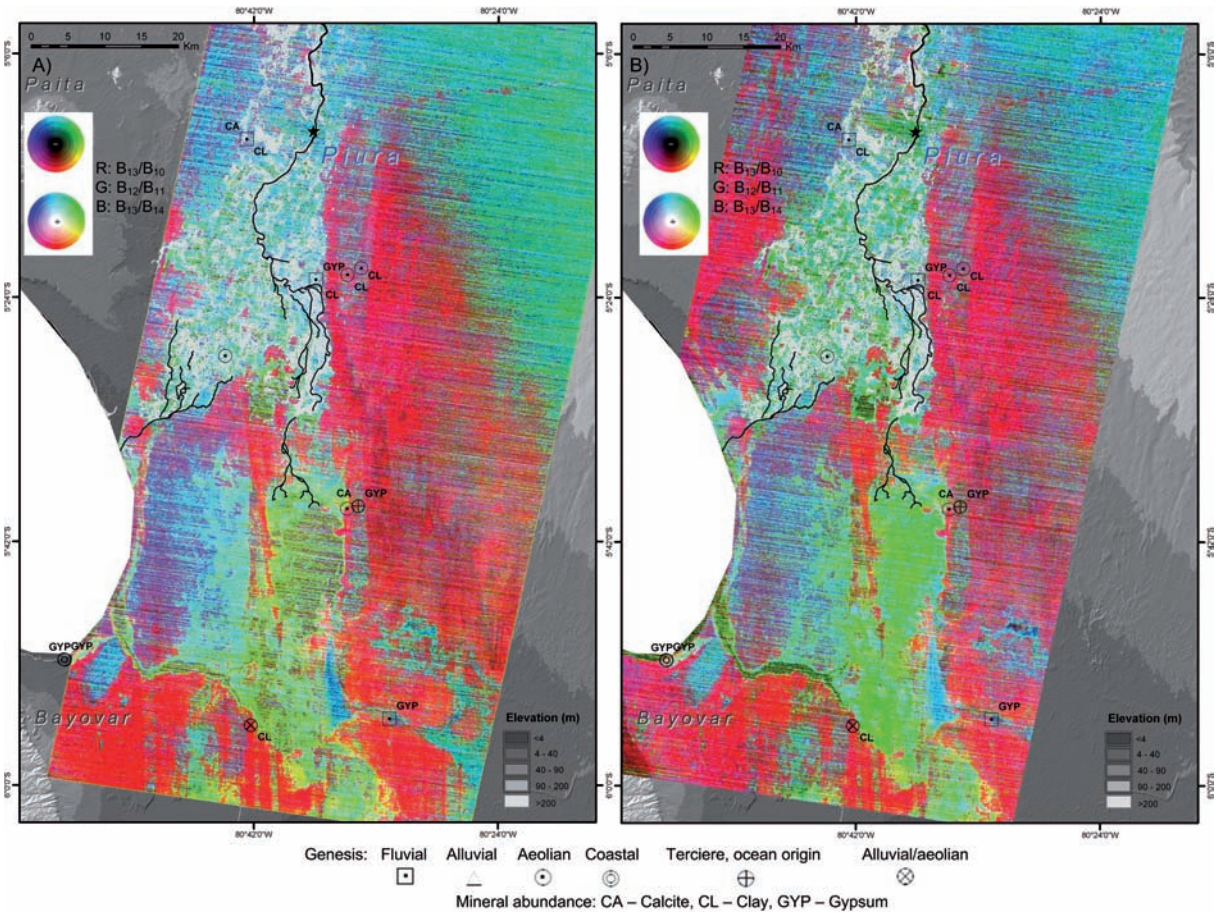

Plate 5: Aster TIR analysis: Mineralogical band ratios for Aster scenes from 05/2006 – wet season (A) and 01/2007 – dry season (B). In grey is a vegetation mask.

Planche 5 : *Analyse des données ASTER TIR: rapports de bandes ASTER montrant la minéralogie pour mai 2006 – saison humide (A) et janvier 2007 – saison sèche (B). La végétation est masquée (gris).*

ARTICLE PAGE 64, V. KOPAČKOVÁ *et Coll.*

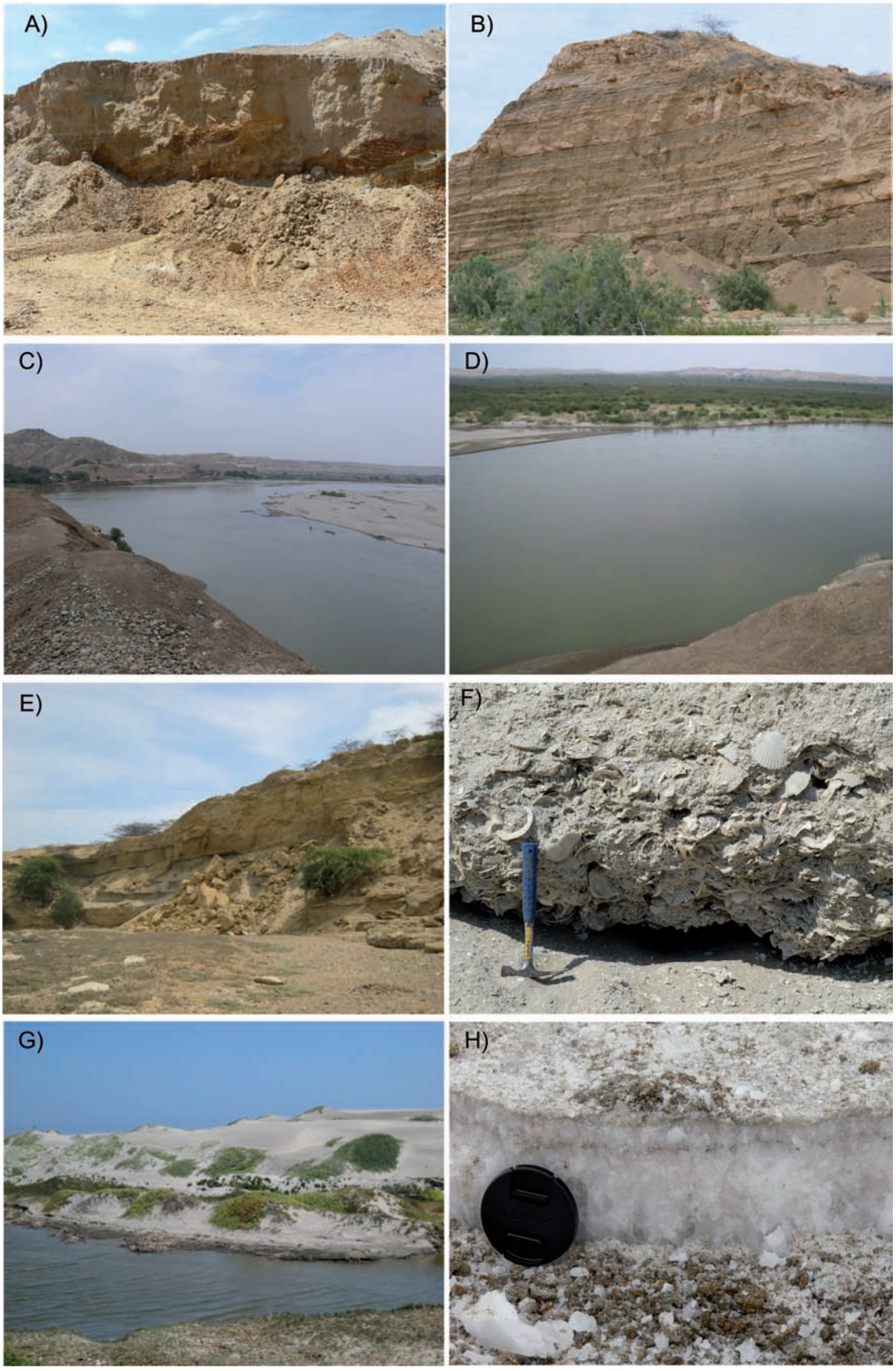

Plate 6: Field photos of the major surface materials: alluvial sediments (A), Cenozoic siliciclastics (B), Chira river (C, D), bioclastics "Tablazos" (E, G), Aeolian sediments along the Oceanside (G), Evaporites – detail (H).

Planche 6 : *Photographies de terrain montrant les dépôts alluviaux de surface (A), roches silicoclastiques cénozoïques (B), le fleuve Chira (C, D), roches bioclastiques « Tablazos » (E, G), sédiments éoliens le long de l'océan (G), Evaporites – détail (H).*

ARTICLE PAGE 64, V. KOPAČKOVÁ *et Coll.*

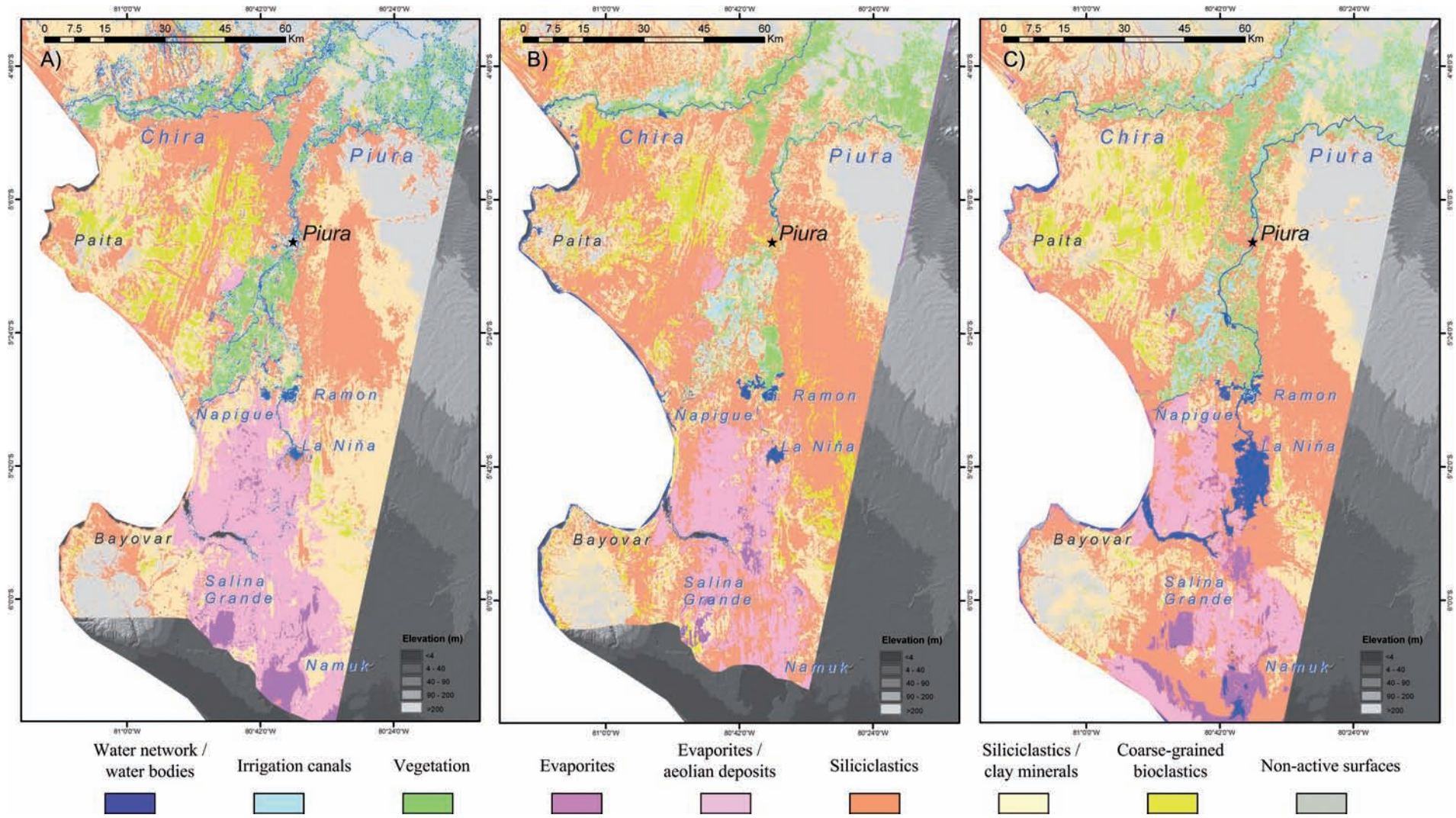

Plate 7: Landcover classifications of Landsat TM images from 1985 (A), 1990 (B) and 2000/2001 (C).

Planche 7 : *Classification de l'occupation des sols à partir de Landsat TM pour 1985 (A), 1990 (B) et 2000/2001 (C).*

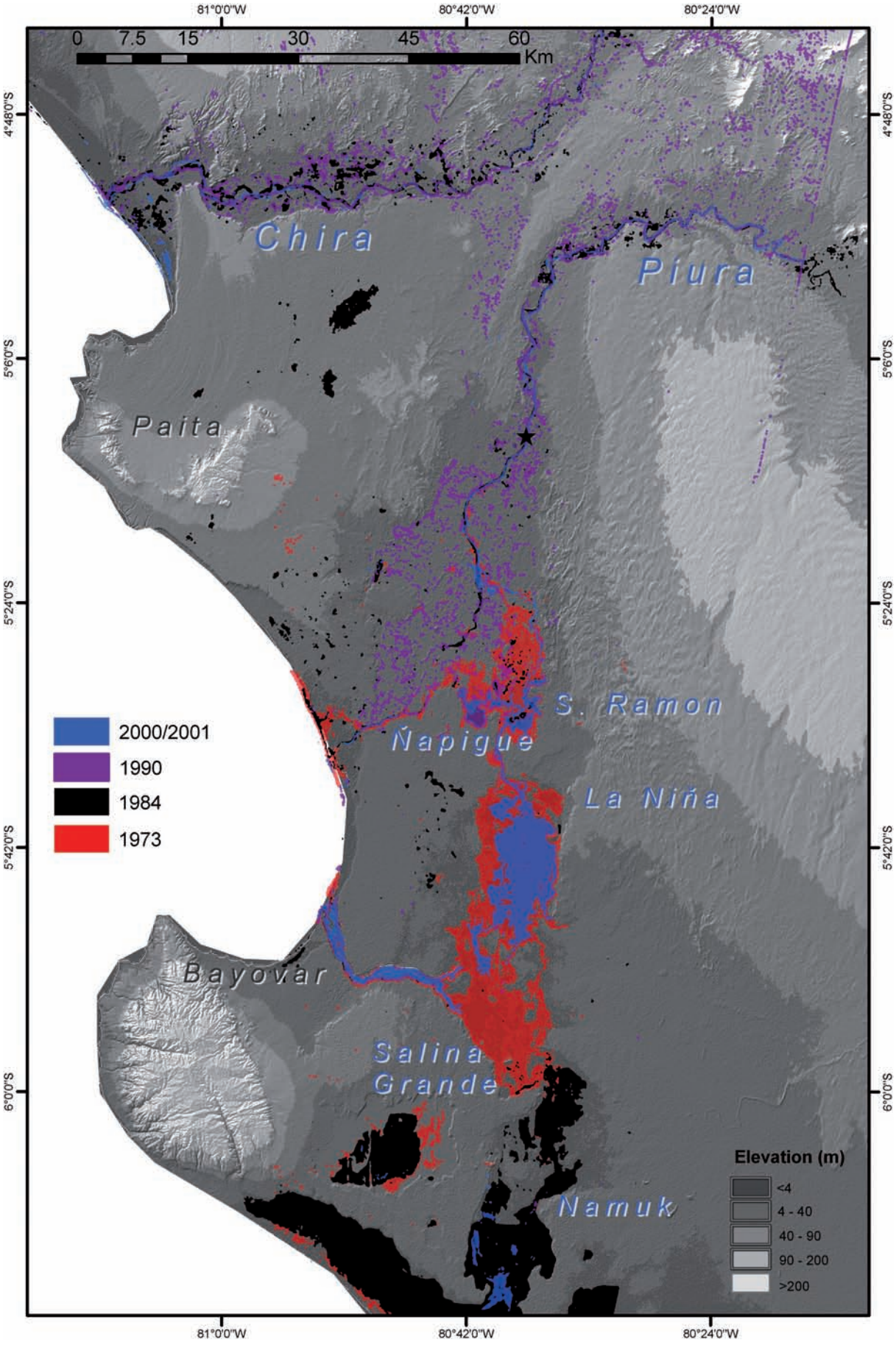

Plate 8: Changes in geometry/position of the river channels and extent of the lakes (1973- 2000/2001).
Planche 8 : *Modification dans la géométrie des chenaux de rivière et extension des lacs (1973- 2000/2001).*

ARTICLE PAGE 64, V. KOPAČKOVÁ *et Coll.*